Electronic Supplementary Material (ESI) for Analyst.

2D analysis of polydisperse core-shell nanoparticles using analytical ultracentrifugation

Supporting Information

Johannes Walter,[a,b] Gary Gorbet,[c] Tugce Akdas,[a,b] Doris Segets,[a,b] Borries Demeler,[c,] Wolfgang Peukert[a,b,*]*

[a] Institute of Particle Technology (LFG), Friedrich-Alexander-Universität Erlangen-Nürnberg (FAU), Cauerstr. 4, 91058 Erlangen, Germany

[b] Interdisciplinary Center for Functional Particle Systems (FPS), Friedrich-Alexander-Universität Erlangen-Nürnberg (FAU), Haberstr. 9a, 91058 Erlangen, Germany

[c] Department of Biochemistry, The University of Texas Health Science Center at San Antonio, 7703 Floyd Curl Drive, San Antonio, Texas 78229-3901, USA

1 Determination of effective partial specific volumes

The basic strategy pursued in our work is to calculate the effective partial specific volume for particles of known shape. We know that the particles are spherical in our case:

$$\frac{f}{f_0} = \left(\frac{f}{f_0}\right)_{shape} = 1 \quad \rightarrow \quad d_{V,eff} = d_{p,eff} = d_h \tag{1}$$

$d_{V,eff}$ is the effective volume equivalent diameter of the particle including the solvation layer, $d_{p,eff}$ is the diameter as given by Stokes' equation and d_h is the hydrodynamic diameter. From the Stokes–Einstein equation it follows:

$$d_{p,eff} = \frac{k_B T}{3\pi\eta D} \tag{2}$$

D is the diffusion coefficient of the particle, k_B is the Boltzmann constant and η is the viscosity of the solvent. Together with the force balance of sedimentation this leads to:

$$\frac{V_{p,eff}}{s}\left(\rho_{p,eff} - \rho_s\right) - f = 0 \tag{3}$$

$$\frac{d_{p,eff}^3 \pi}{6s}\left(\rho_{p,eff} - \rho_s\right) - 3\pi\eta d_{p,eff} = 0 \tag{4}$$

$$\frac{d_{p,eff}^2}{6s}\left(\rho_{p,eff} - \rho_s\right) = 3\eta \tag{5}$$

$$d_{p,eff}^2\left(\rho_{p,eff} - \rho_s\right) = 18\eta s \tag{6}$$

$$\rho_{p,eff} = \frac{1}{\bar{v}_{p,eff}} = \frac{18\eta s}{d_{p,eff}^2} + \rho_s \tag{7}$$

$V_{p,eff}$ is the effective volume of the particle including all contributions from the shell, $\rho_{p,eff}$ is the corresponding density and ρ_s is the density of the displaced solvent. These correlations allow calculating the effective partial specific volume of the solvated particle by using the sedimentation coefficient as well as the diameter of the effective particle determined by its diffusion coefficient.

For the given case s and $\bar{\nu}_{p,eff}$ were used for parametrization. $\bar{\nu}_{p,eff}$ and s allow calculation of the corresponding D values *via* Equations 2 and 7. Both, s and D are then fitted using Lamm's equation. It has to be taken into account that $\bar{\nu}_{p,eff}$ includes the solvation layer. By definition, the f/f_0 obtained by using $\bar{\nu}_{p,eff}$ is always equal to $(f/f_0)_{shape}$ and therefore equals unity for this given case of spherical particles because the volume expansion is not attributed to the frictional ratio but included in $\bar{\nu}_{p,eff}$.

2 Influence of shape anisotropy on partial specific volumes and shell thicknesses

The determination of effective partial specific volumes *via* the 2D approach as described in the previous section relies on the exact knowledge of the shape anisotropy. In case detailed knowledge on shape is not available, sedimentation and diffusion data derived by AUC could be misinterpreted. This will result in incorrect effective partial specific volumes and shell thicknesses. In the following section, possible errors will be estimated based on a case study.

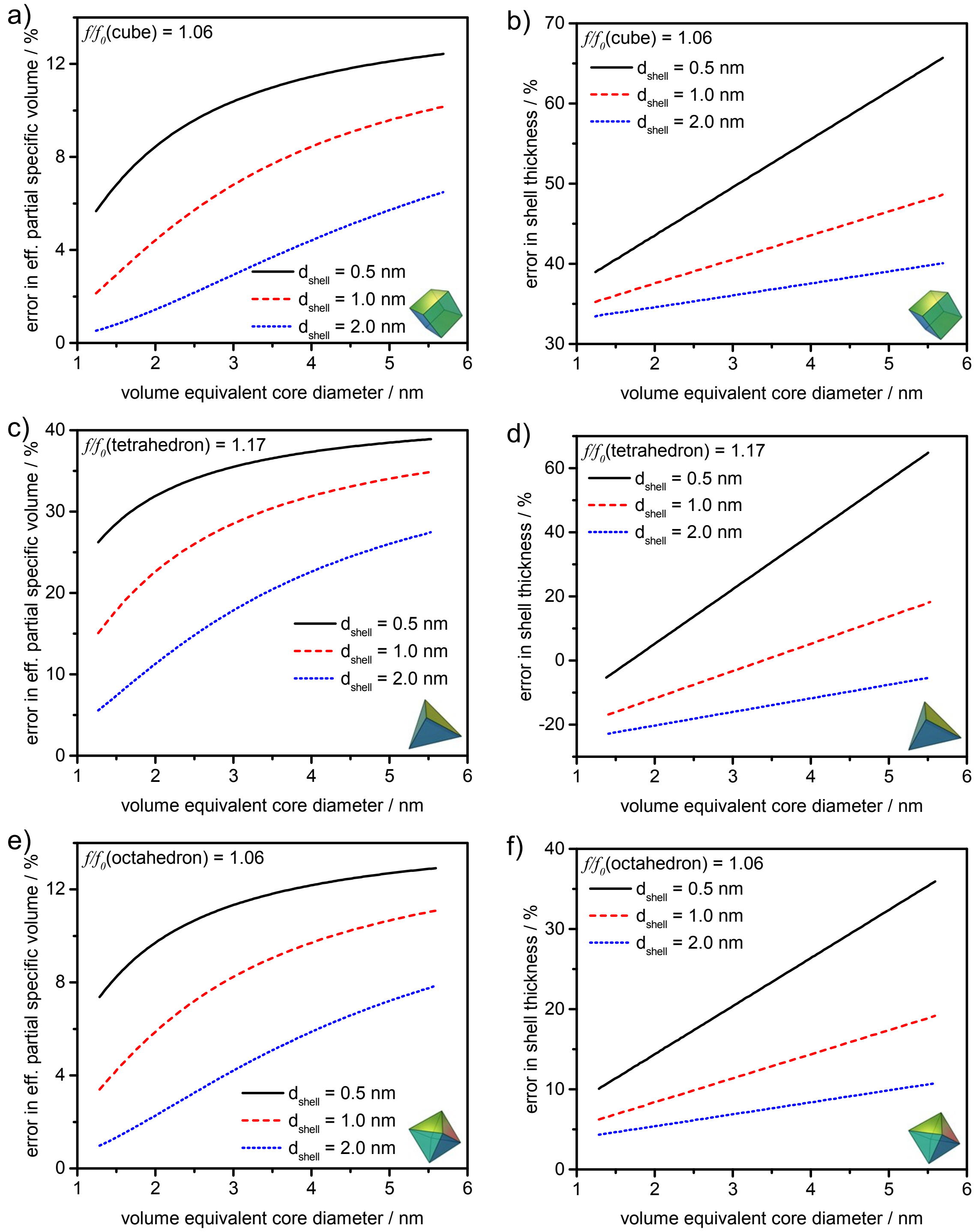

Figure S1. Errors in the effective partial specific volumes and shell thicknesses for cubes, tetrahedrons and octahedrons as a function of the volume equivalent core diameters.

For the error calculations it was assumed that particles of fixed core density (5 g/cm^3) carry a shell of certain thickness (0.5 nm, 1.0 nm or 2.0 nm). The density of the shell was further set to a fixed value of 1.0 g/cm^3. Moreover, calculations were conducted for water at standard conditions. Next, size parameters, effective partial specific volumes as well as sedimentation and diffusion coefficients were calculated as a function of the volume equivalent core diameter for particles of cubical, tetrahedral and octahedral shape. The frictional ratios for the three different geometries were taken from Hubbard *et al.*[1]

Based on the sedimentation and diffusion coefficients, the effective partial specific volumes as would be obtained by a 2D analysis were calculated by assuming spherical shape. Moreover, the corresponding shell thicknesses were fitted. By comparing this data to the original data, the shape induced errors could be calculated. The errors for the effective partial specific volumes and the shell thicknesses are shown in Figure S1 for the three different shapes and varying original shell thicknesses. It was found that the errors always decrease for larger shell thicknesses as the shape induced error in the effective partial specific volume becomes less influencing. Moreover, the errors in the effective partial specific volumes and shell thicknesses were found to be the highest for the tetrahedron as it has the largest frictional ratio (1.17) and lowest sphericity (0.671). The sphericity can be defined as the surface area of a sphere of the same volume as the particle divided by the actual surface area of that particle. Smaller values indicate that the actual body deviates more significantly from a sphere. As a consequence, the relative volume of the shell compared to the core volume will increase with decreasing sphericity as the surface area to volume ratio is the lowest for the sphere. The cube as well as the octahedron has a frictional ratio of 1.06. However, the error in the shell thickness was found to be less for the octahedron as it has a larger sphericity (0.846) compared to the cube (0.806).

3 Simulated models #1 – #3

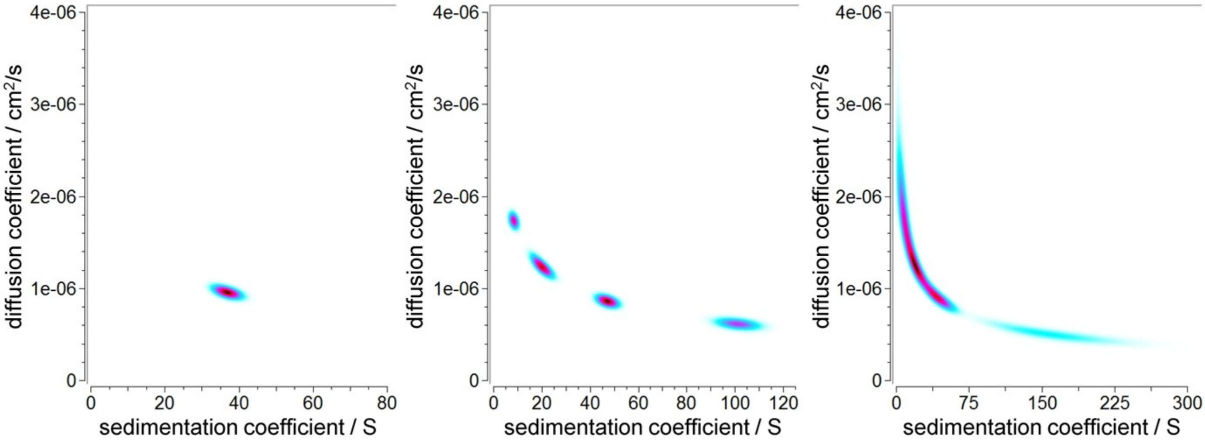

Figure S2. Simulated 2D distributions for models #1 – #3 represented as sedimentation versus diffusion coefficients.

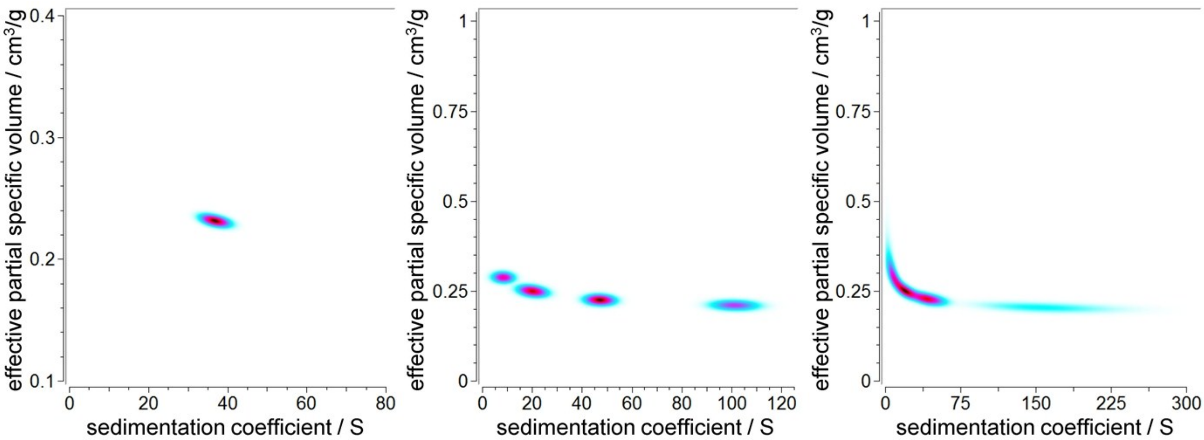

Figure S3. Simulated 2D distributions for models #1 – #3 represented as sedimentation coefficients versus partial specific volumes.

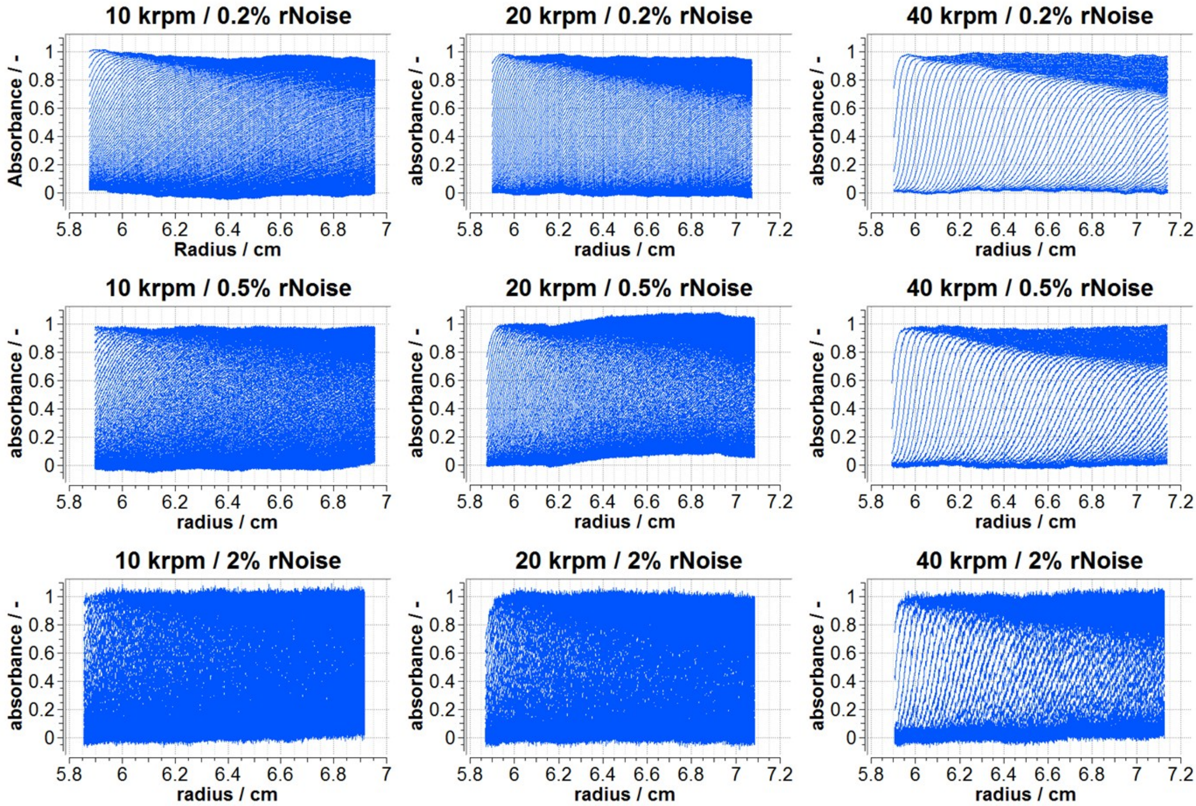

Figure S4. Simulated SV data for model #1 with different rotor speeds and levels of random noise.

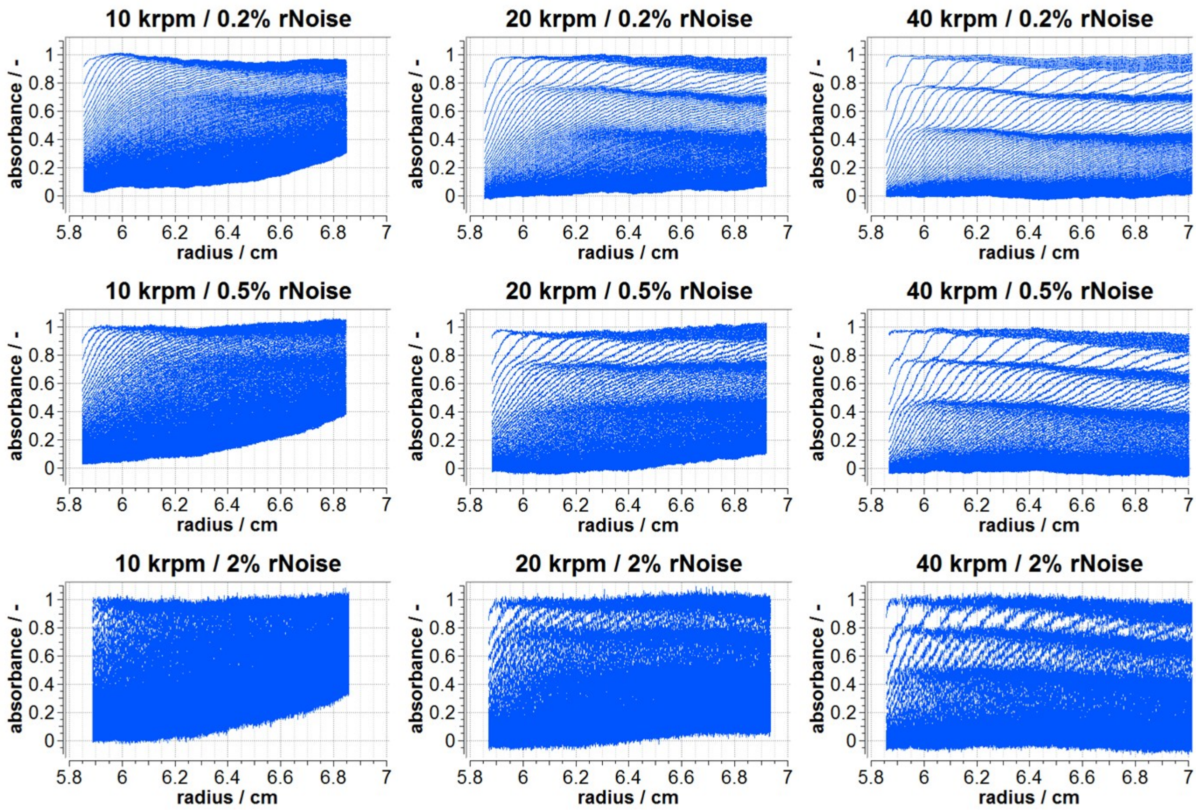

Figure S5. Simulated SV data for model #2 with different rotor speeds and levels of random noise.

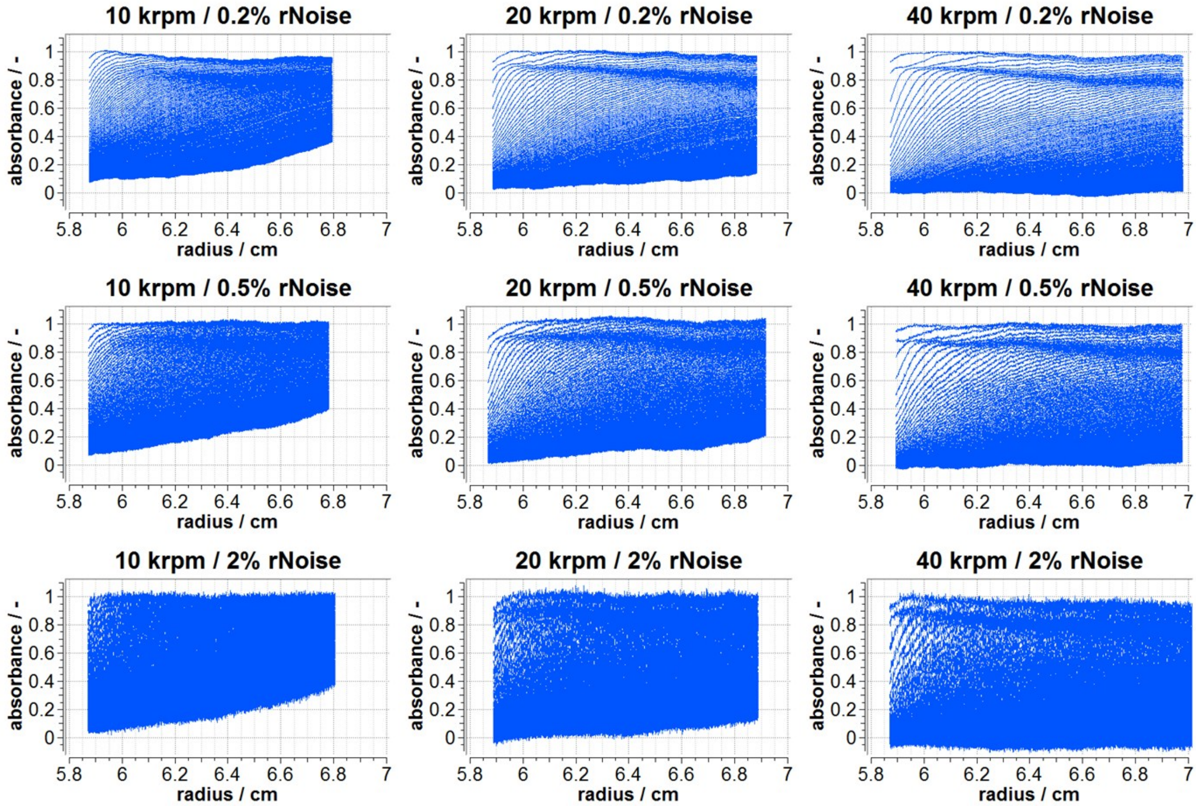

Figure S6. Simulated SV data for model #3 with different rotor speeds and levels of random noise.

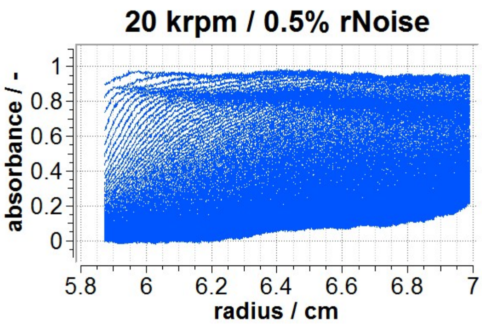

Figure S7. Simulated SV data for model #4.

4 Shell thickness function of model #4

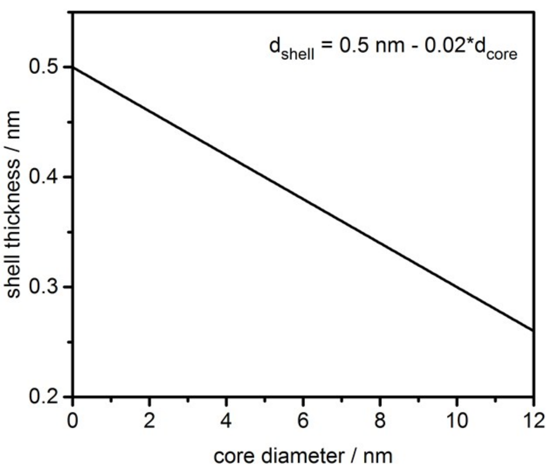

Figure S8. Shell thickness in model #4 as a function of the core diameter.

5 Results of 1D c(s) analyses

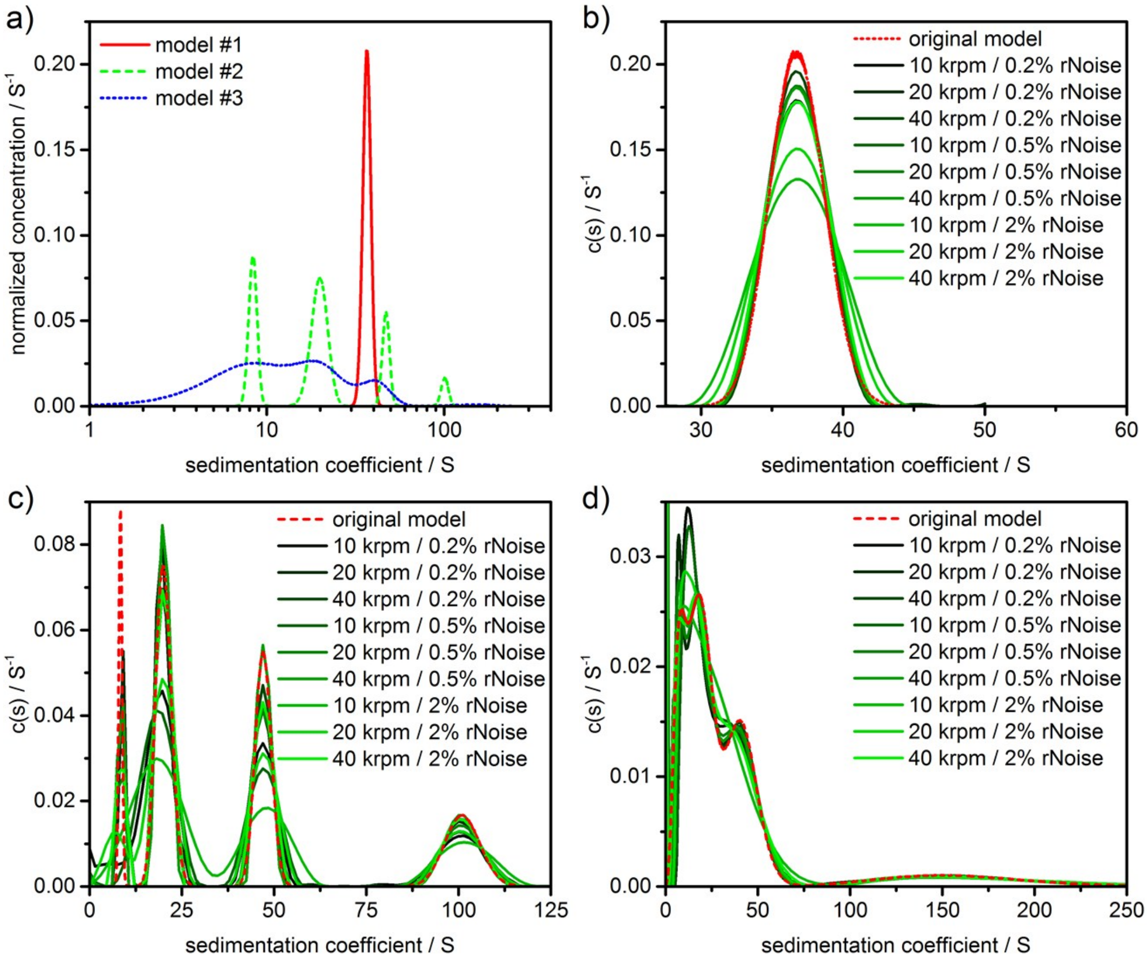

Figure S9. Original models #1 – #3 reduced to the s-dimension in logarithmic scaling (a) and results of the c(s) analyses for model #1 (b), model #2 (c), and model #3 (d). Data is shown for varying random noise and rotor speeds. The original model is shown in b) – d) by a red dashed line.

6 2D analyses of sedimentation and diffusion coefficients for model #1

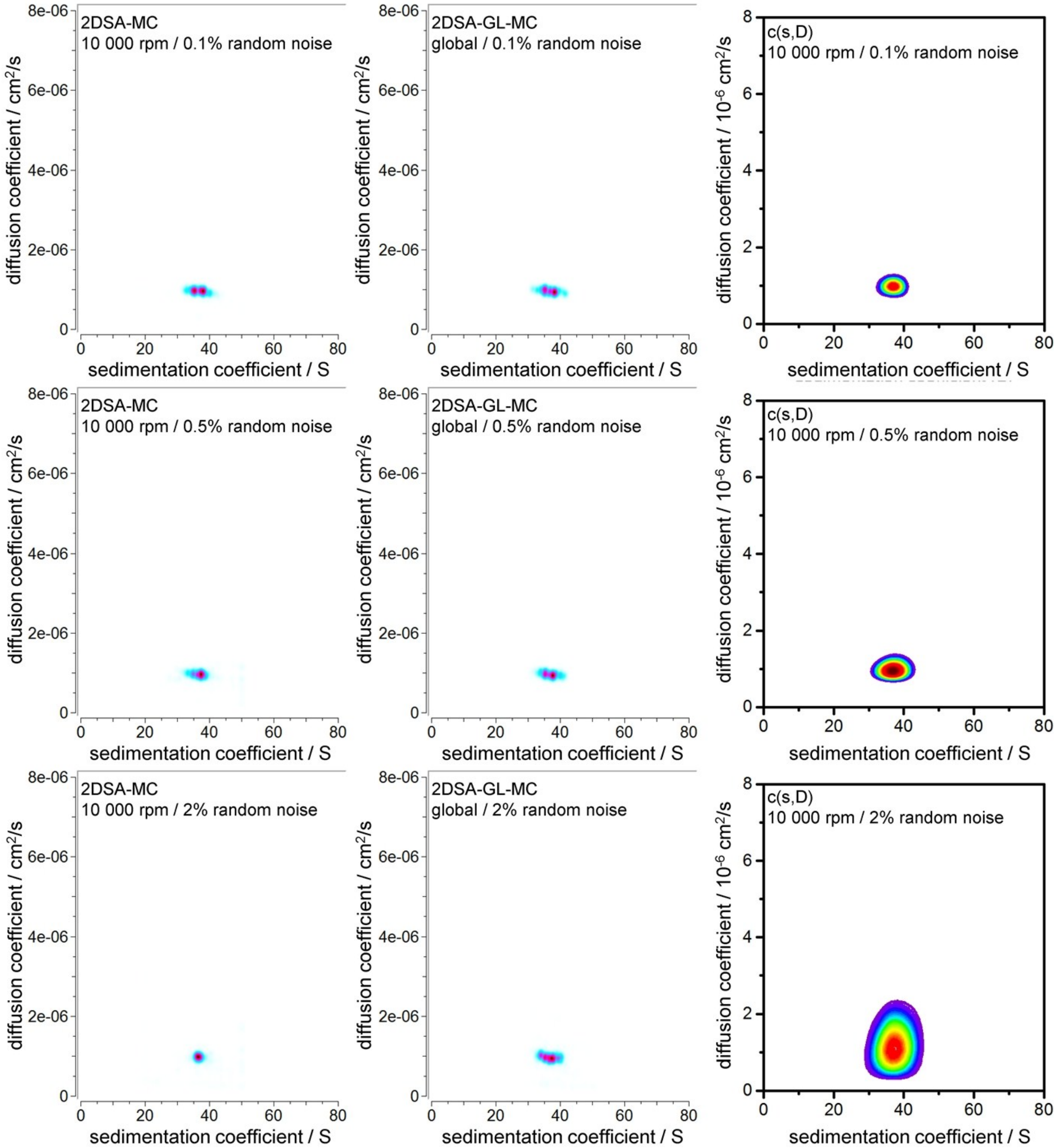

Figure S10. Results of the 2DSA-MC, global speed 2DSA-MC and c(s,D) analyses shown from left to right for model #1. Results are shown for a rotor speed of 10,000 rpm (except the global speed approach which is a combined analysis at rotor speeds of 10,000 rpm, 20,000 rpm and 40,000 rpm). The random noise is varied top down. The original simulated model to be reproduced (target) is shown in Figure S1.

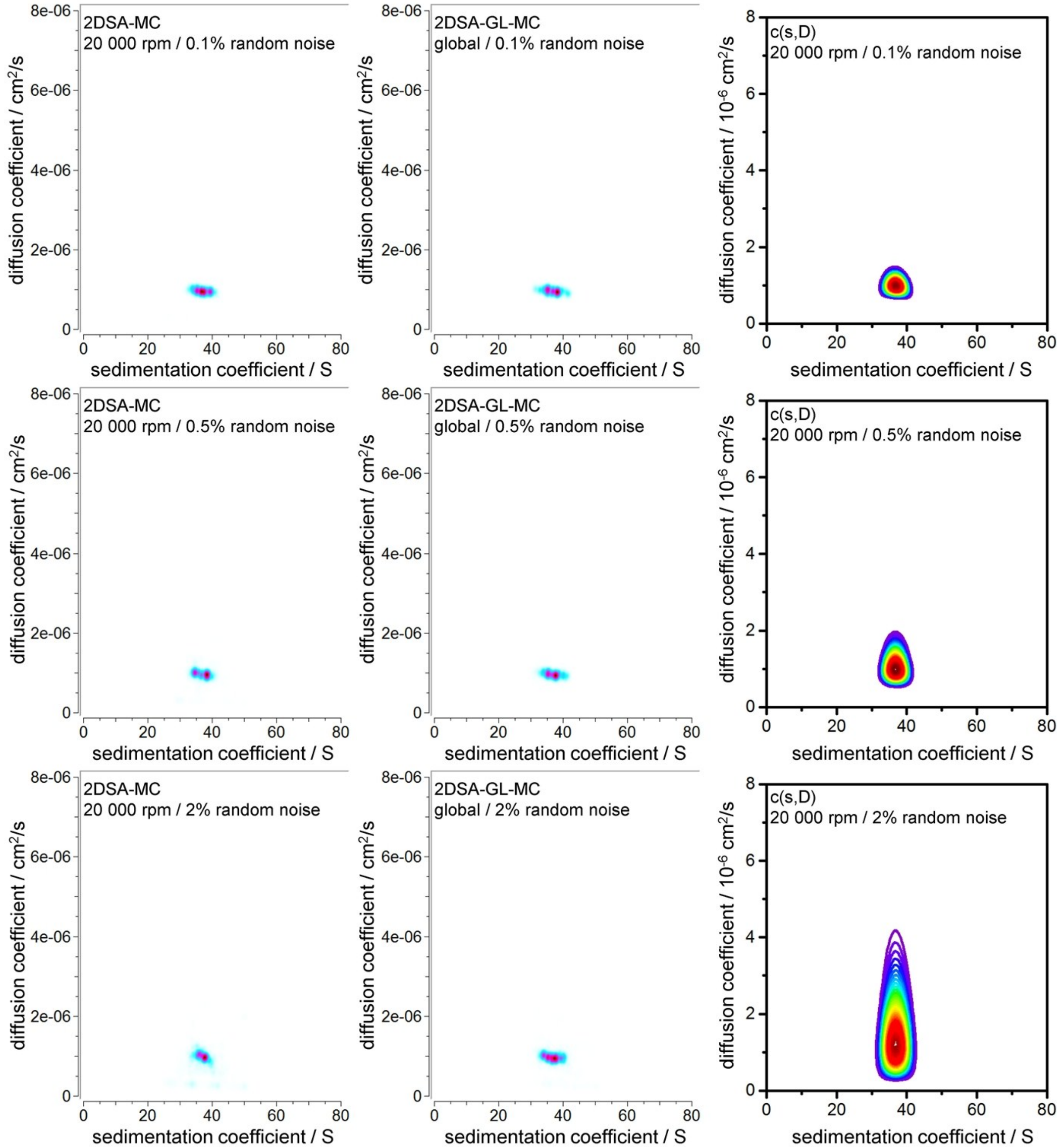

Figure S11. Results of the 2DSA-MC, global speed 2DSA-MC and c(s,D) analyses shown from left to right for model #1. Results are shown for a rotor speed of 20,000 rpm (except the global speed approach which is a combined analysis at rotor speeds of 10,000 rpm, 20,000 rpm and 40,000 rpm). The random noise is varied top down. The original simulated model to be reproduced (target) is shown in Figure S1.

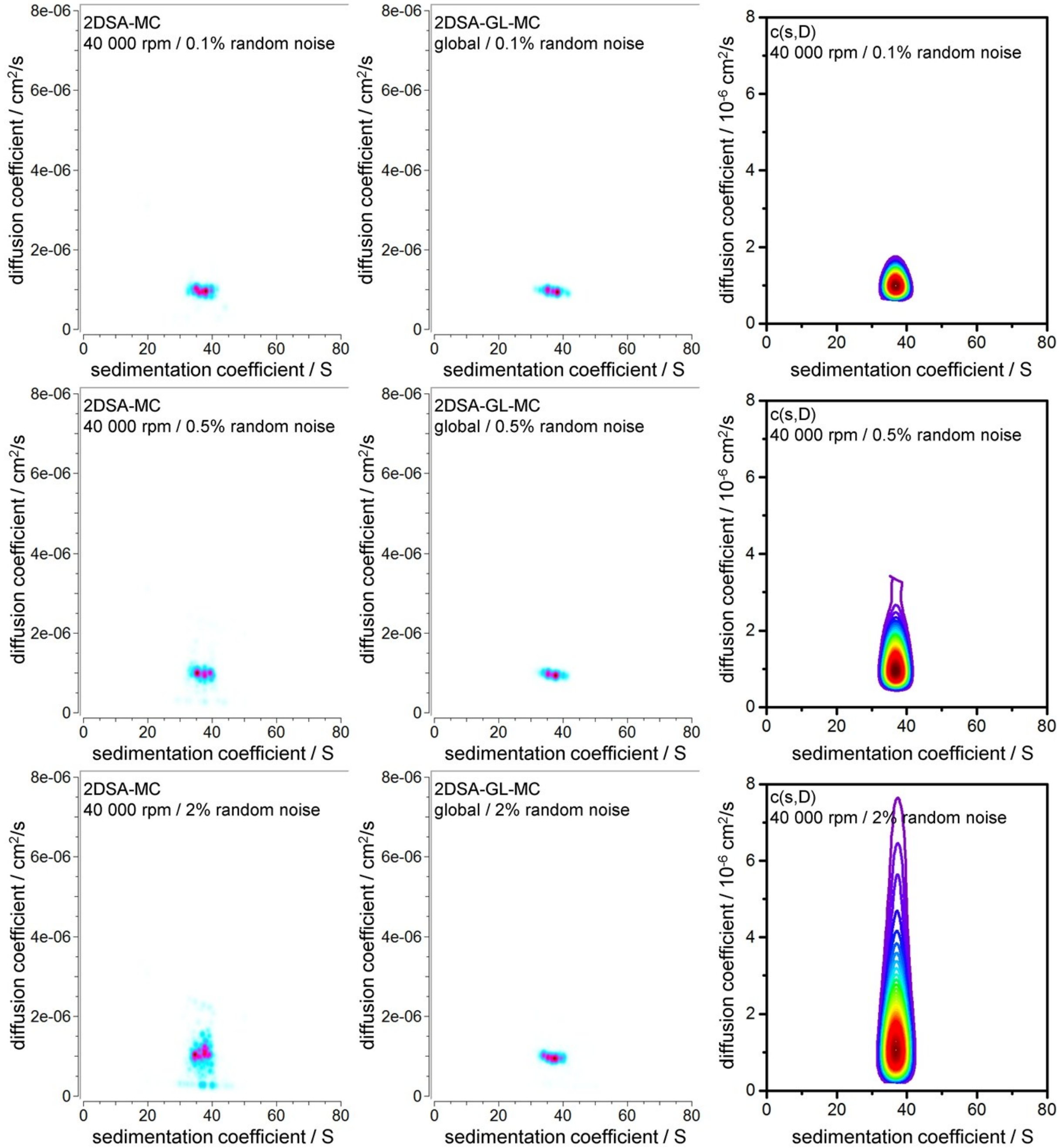

Figure S12. Results of the 2DSA-MC, global speed 2DSA-MC and c(s,D) analyses shown from left to right for model #1. Results are shown for a rotor speed of 40,000 rpm (except the global speed approach which is a combined analysis at rotor speeds of 10,000 rpm, 20,000 rpm and 40,000 rpm). The random noise is varied top down. The original simulated model to be reproduced (target) is shown in Figure S1.

7 2D analyses of sedimentation and diffusion coefficients for model #2

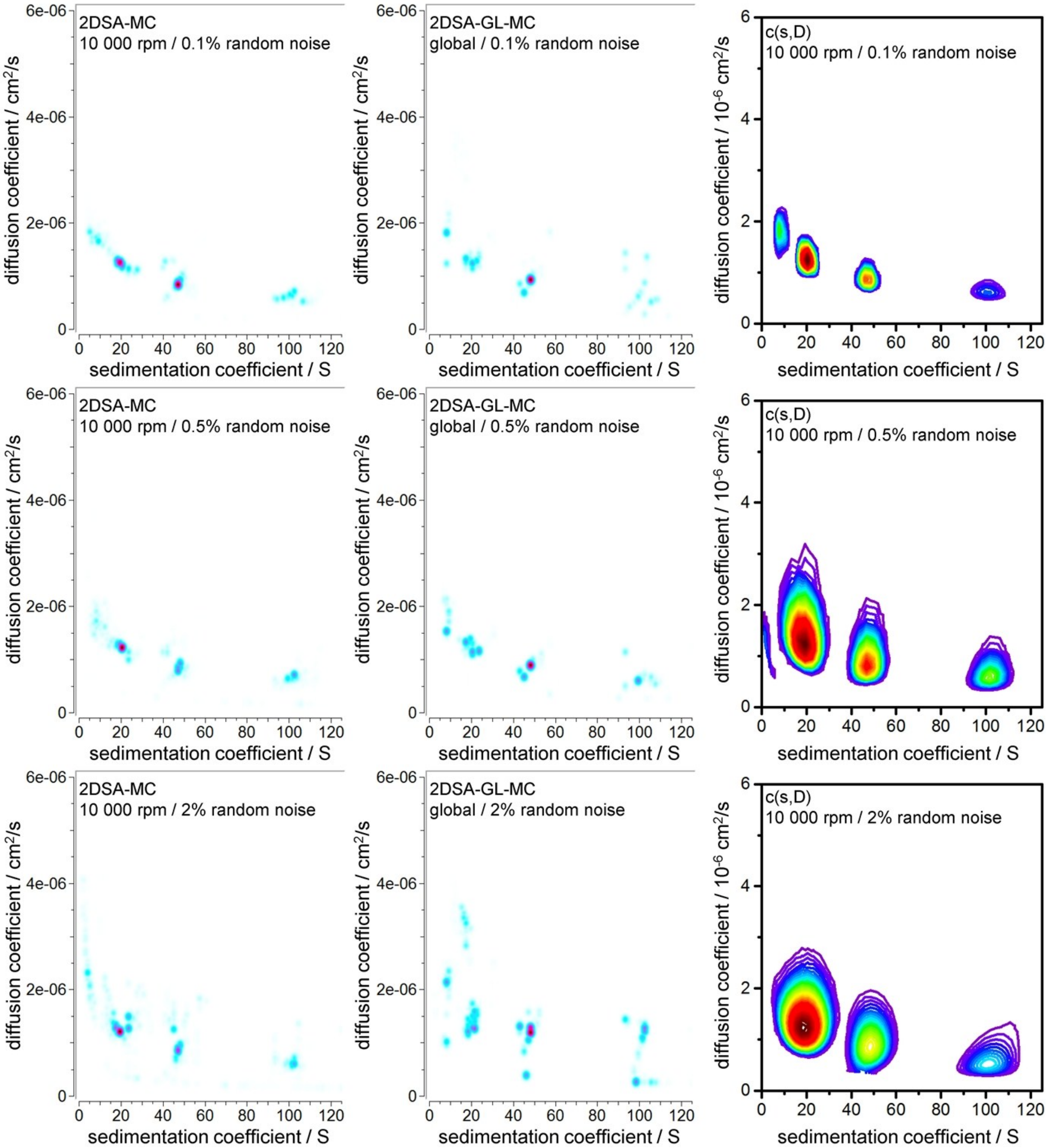

Figure S13. Results of the 2DSA-MC, global speed 2DSA-MC and c(s,D) analyses shown from left to right for model #2. Results are shown for a rotor speed of 10,000 rpm (except the global speed approach which is a combined analysis at rotor speeds of 10,000 rpm, 20,000 rpm and 40,000 rpm). The random noise is varied top down. The original simulated model to be reproduced (target) is shown in Figure S1.

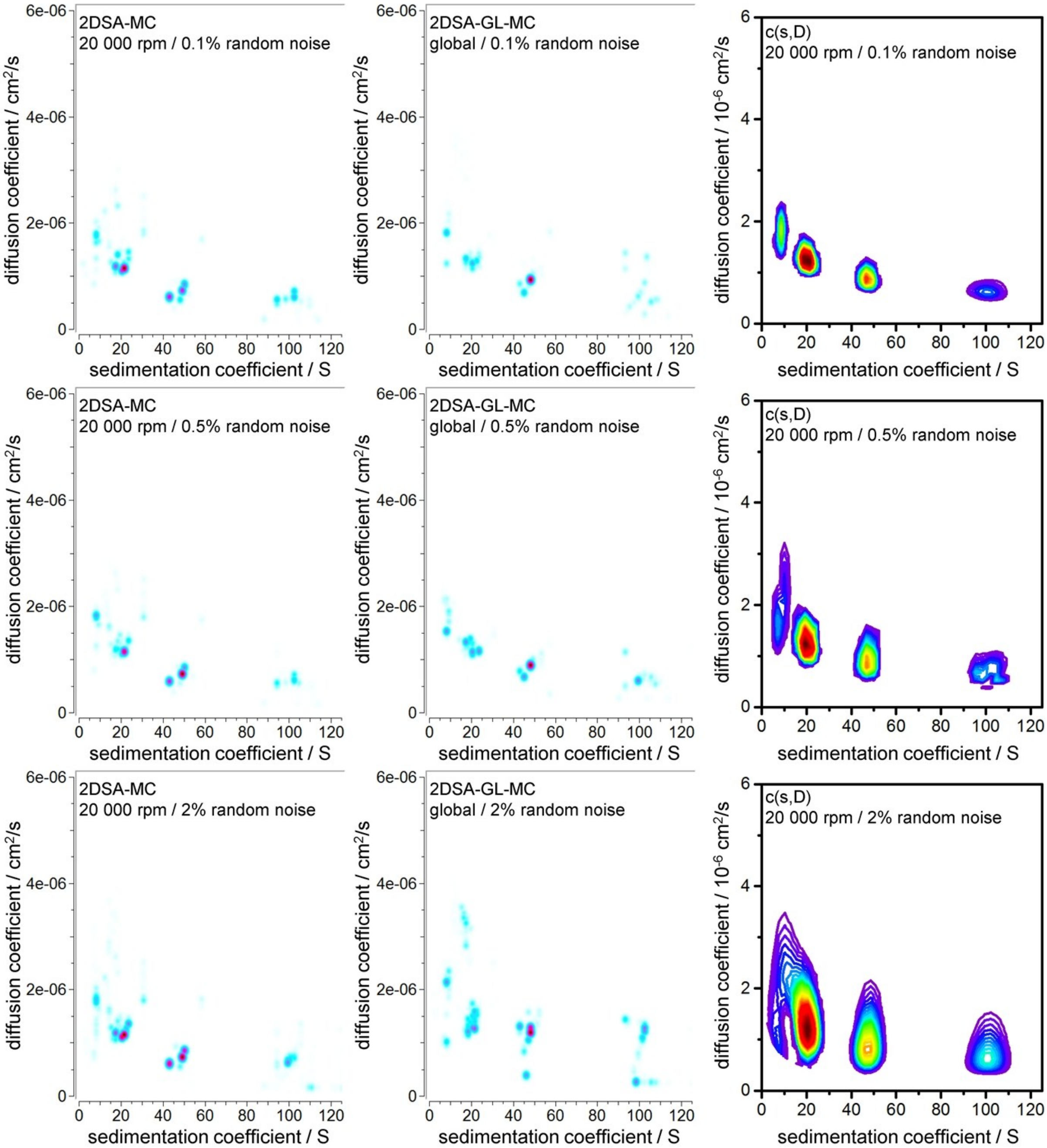

Figure S14. Results of the 2DSA-MC, global speed 2DSA-MC and c(s,D) analyses shown from left to right for model #2. Results are shown for a rotor speed of 20,000 rpm (except the global speed approach which is a combined analysis at rotor speeds of 10,000 rpm, 20,000 rpm and 40,000 rpm). The random noise is varied top down. The original simulated model to be reproduced (target) is shown in Figure S1.

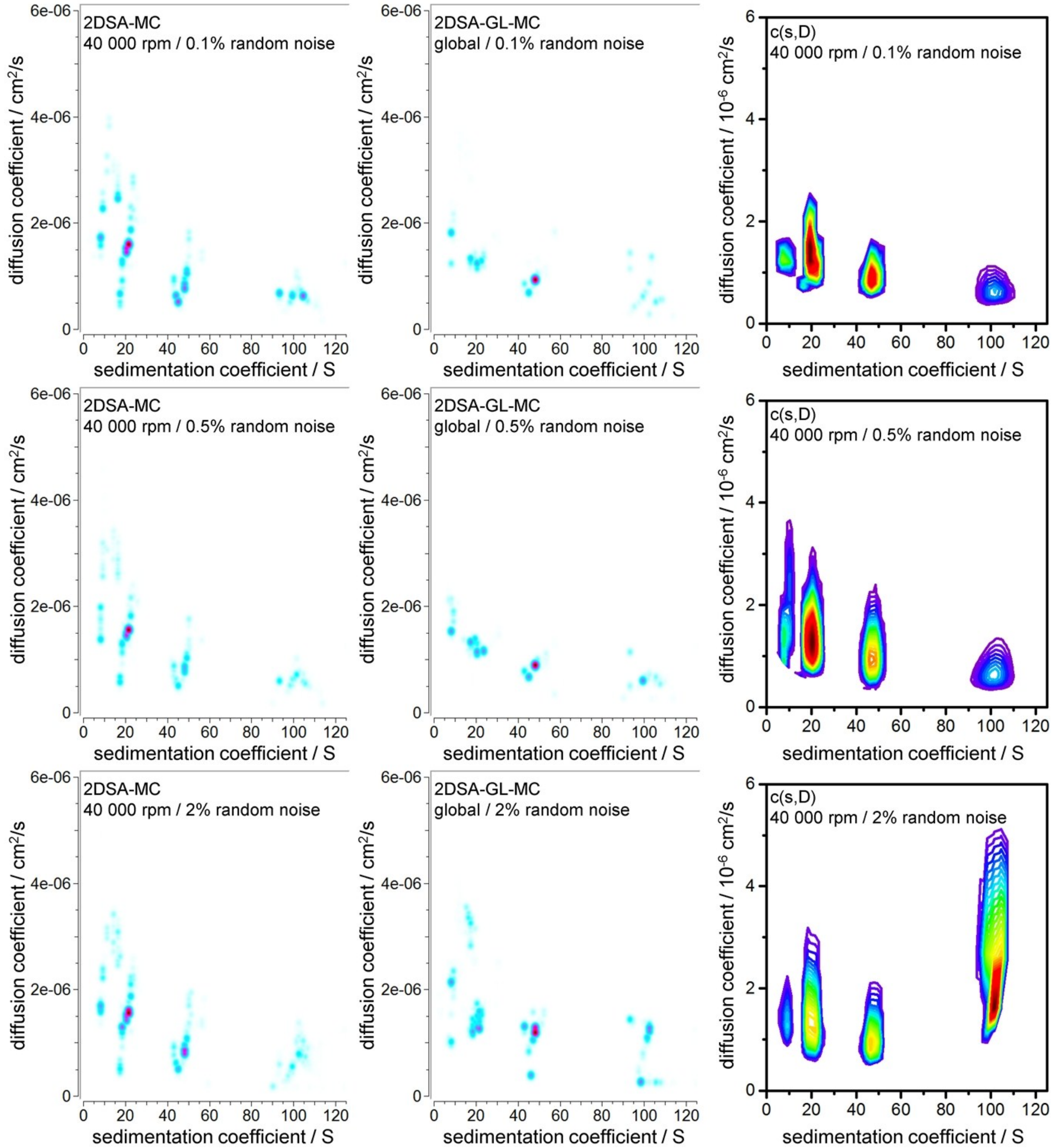

Figure S15. Results of the 2DSA-MC, global speed 2DSA-MC and c(s,D) analyses shown from left to right for model #2. Results are shown for a rotor speed of 40,000 rpm (except the global speed approach which is a combined analysis at rotor speeds of 10,000 rpm, 20,000 rpm and 40,000 rpm). The random noise is varied top down. The original simulated model to be reproduced (target) is shown in Figure S1.

8 2D analyses of sedimentation and diffusion coefficients for model #3

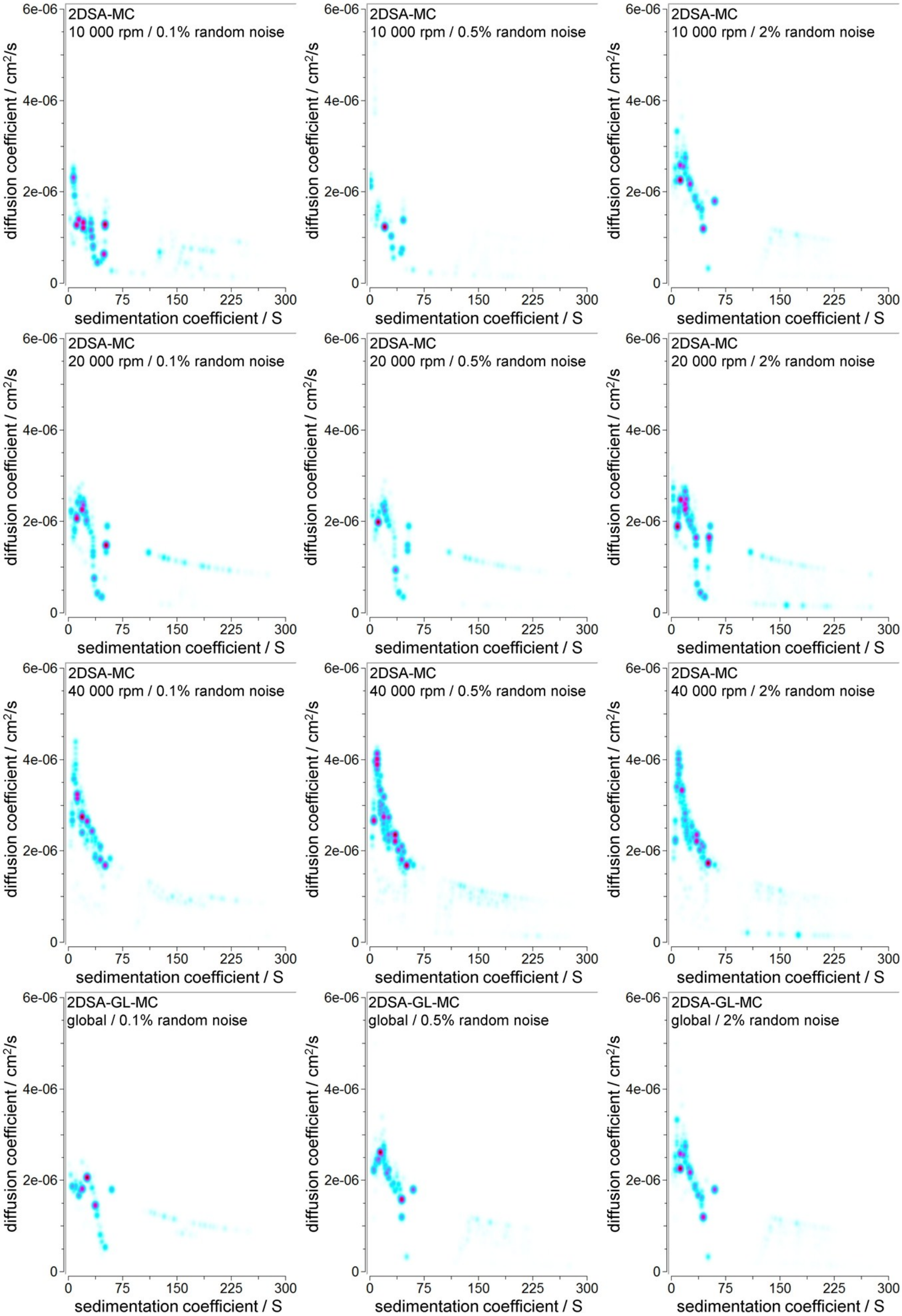

Figure S16. Results of the 2DSA-MC with increasing random noise shown from left to right and increasing rotor speed top down for model #3. The results of the global speed 2DSA-MC are shown in the last row. c(s,D) evaluations could not be performed for model #3 due to significant peak clipping. The original simulated model to be reproduced (target) is shown in Figure S1.

9 2D analyses of sedimentation coefficients and partial specific volumes for model #1

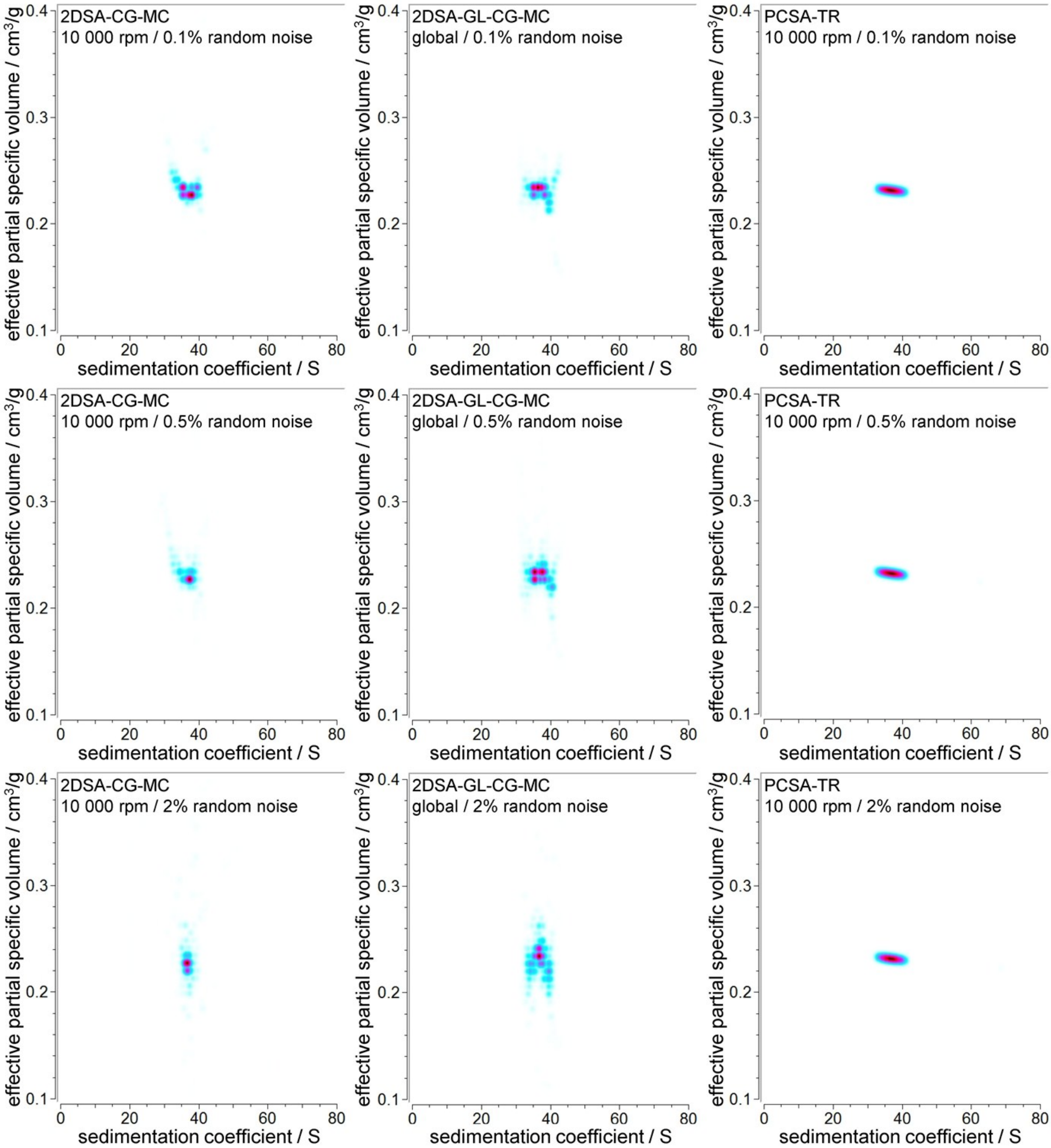

Figure S17. Results of the 2DSA-CG-MC, global speed 2DSA-CG-MC and PCSA-TR shown from left to right for model #1. Results are shown for a rotor speed of 10,000 rpm (except the global speed approach which is a combined analysis at rotor speeds of 10,000 rpm, 20,000 rpm and 40,000 rpm). The random noise is varied top down. The original simulated model to be reproduced (target) is shown in Figure S2.

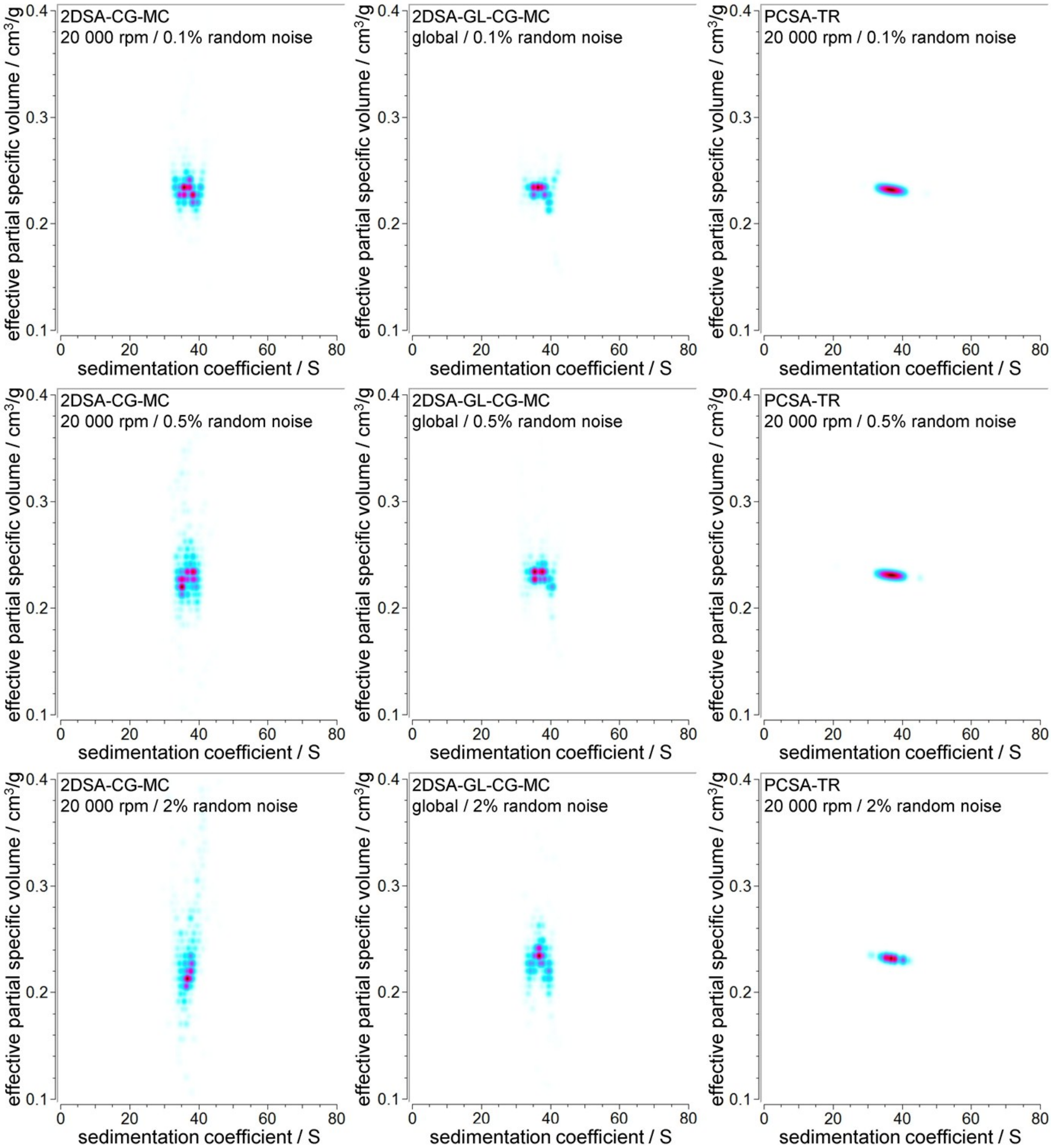

Figure S18. Results of the 2DSA-CG-MC, global speed 2DSA-CG-MC and PCSA-TR shown from left to right for model #1. Results are shown for a rotor speed of 20,000 rpm (except the global speed approach which is a combined analysis at rotor speeds of 10,000 rpm, 20,000 rpm and 40,000 rpm). The random noise is varied top down. The original simulated model to be reproduced (target) is shown in Figure S2.

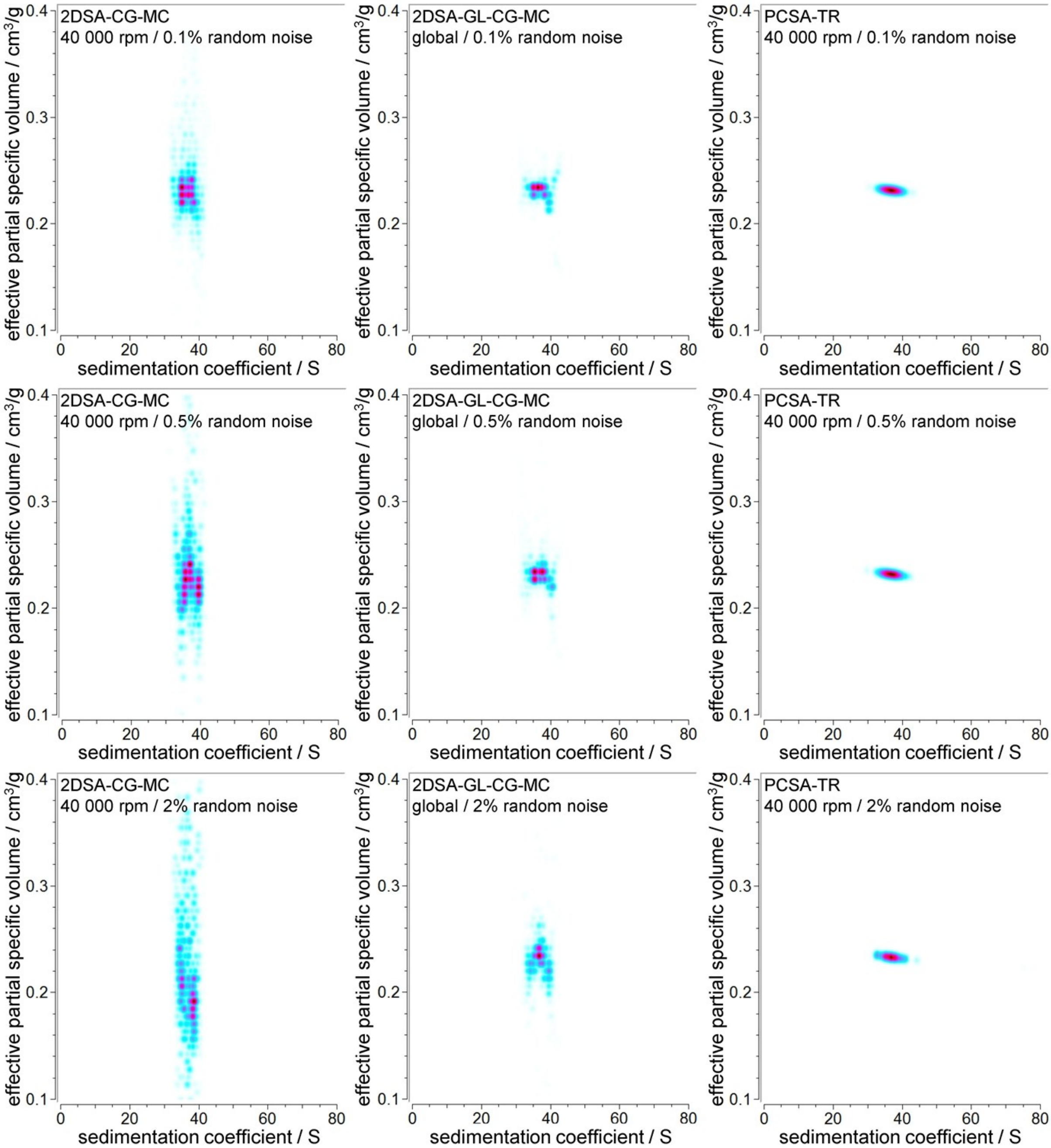

Figure S19. Results of the 2DSA-CG-MC, global speed 2DSA-CG-MC and PCSA-TR shown from left to right for model #1. Results are shown for a rotor speed of 40,000 rpm (except the global speed approach which is a combined analysis at rotor speeds of 10,000 rpm, 20,000 rpm and 40,000 rpm). The random noise is varied top down. The original simulated model to be reproduced (target) is shown in Figure S2.

10 2D analyses of sedimentation coefficients and partial specific volumes for model #2

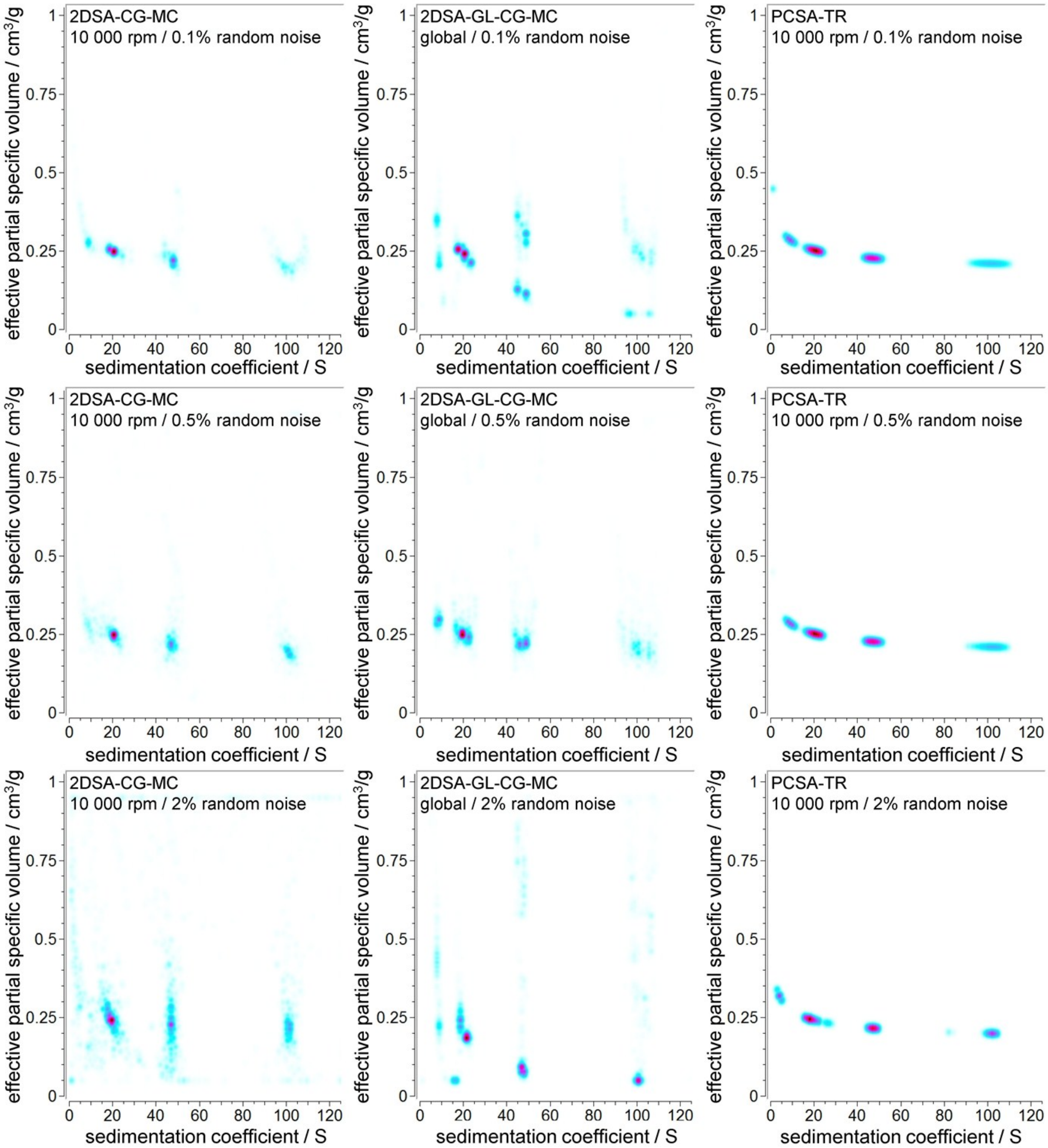

Figure S20. Results of the 2DSA-CG-MC, global speed 2DSA-CG-MC and PCSA-TR shown from left to right for model #2. Results are shown for a rotor speed of 10,000 rpm (except the global speed approach which is a combined analysis at rotor speeds of 10,000 rpm, 20,000 rpm and 40,000 rpm). The random noise is varied top down. The original simulated model to be reproduced (target) is shown in Figure S2.

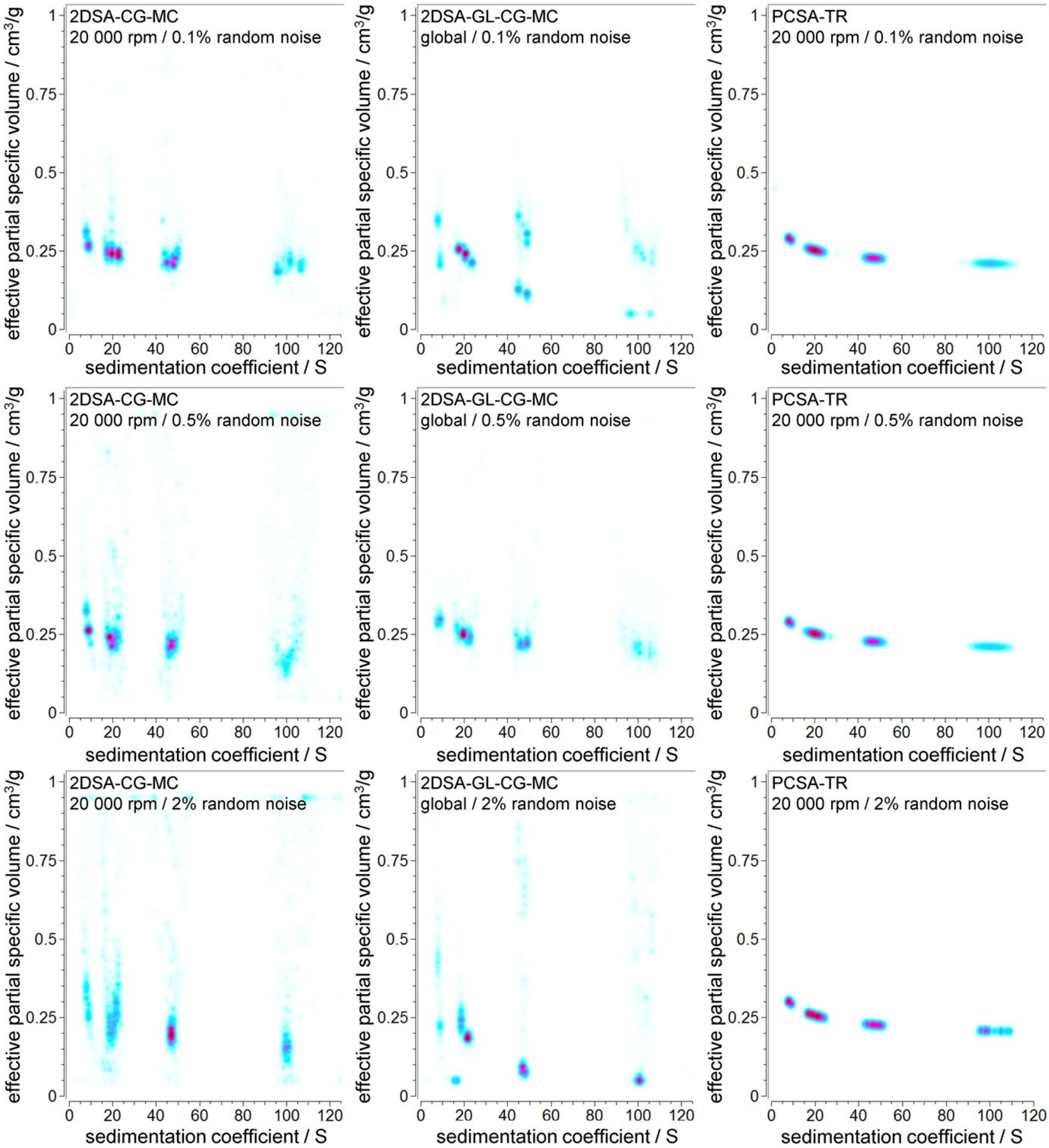

Figure S21. Results of the 2DSA-CG-MC, global speed 2DSA-CG-MC and PCSA-TR shown from left to right for model #2. Results are shown for a rotor speed of 20,000 rpm (except the global speed approach which is a combined analysis at rotor speeds of 10,000 rpm, 20,000 rpm and 40,000 rpm). The random noise is varied top down. The original simulated model to be reproduced (target) is shown in Figure S2.

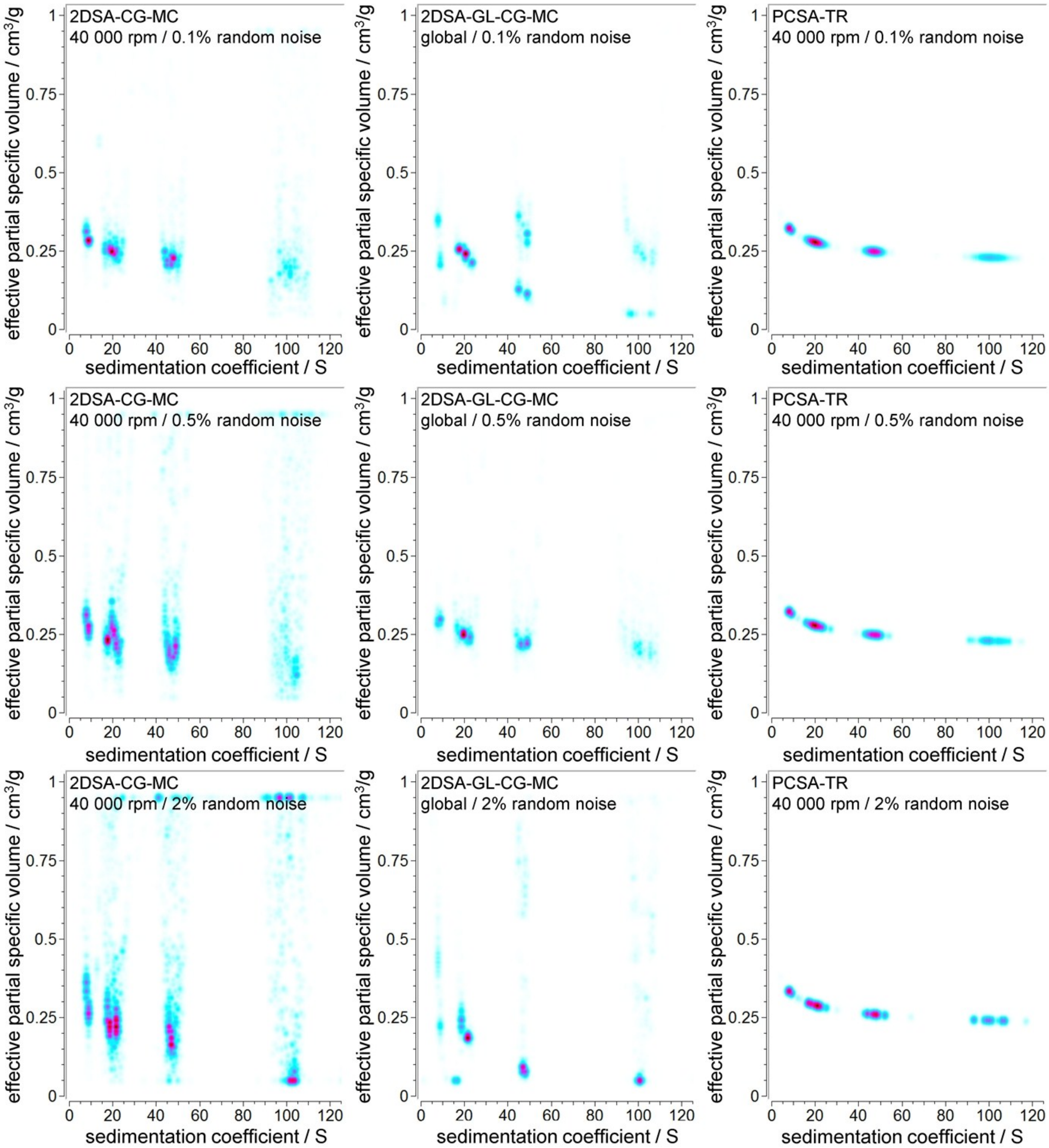

Figure S22. Results of the 2DSA-CG-MC, global speed 2DSA-CG-MC and PCSA-TR shown from left to right for model #2. Results are shown for a rotor speed of 40,000 rpm (except the global speed approach which is a combined analysis at rotor speeds of 10,000 rpm, 20,000 rpm and 40,000 rpm). The random noise is varied top down. The original simulated model to be reproduced (target) is shown in Figure S2.

11 2D analyses of sedimentation coefficients and partial specific volumes for model #3

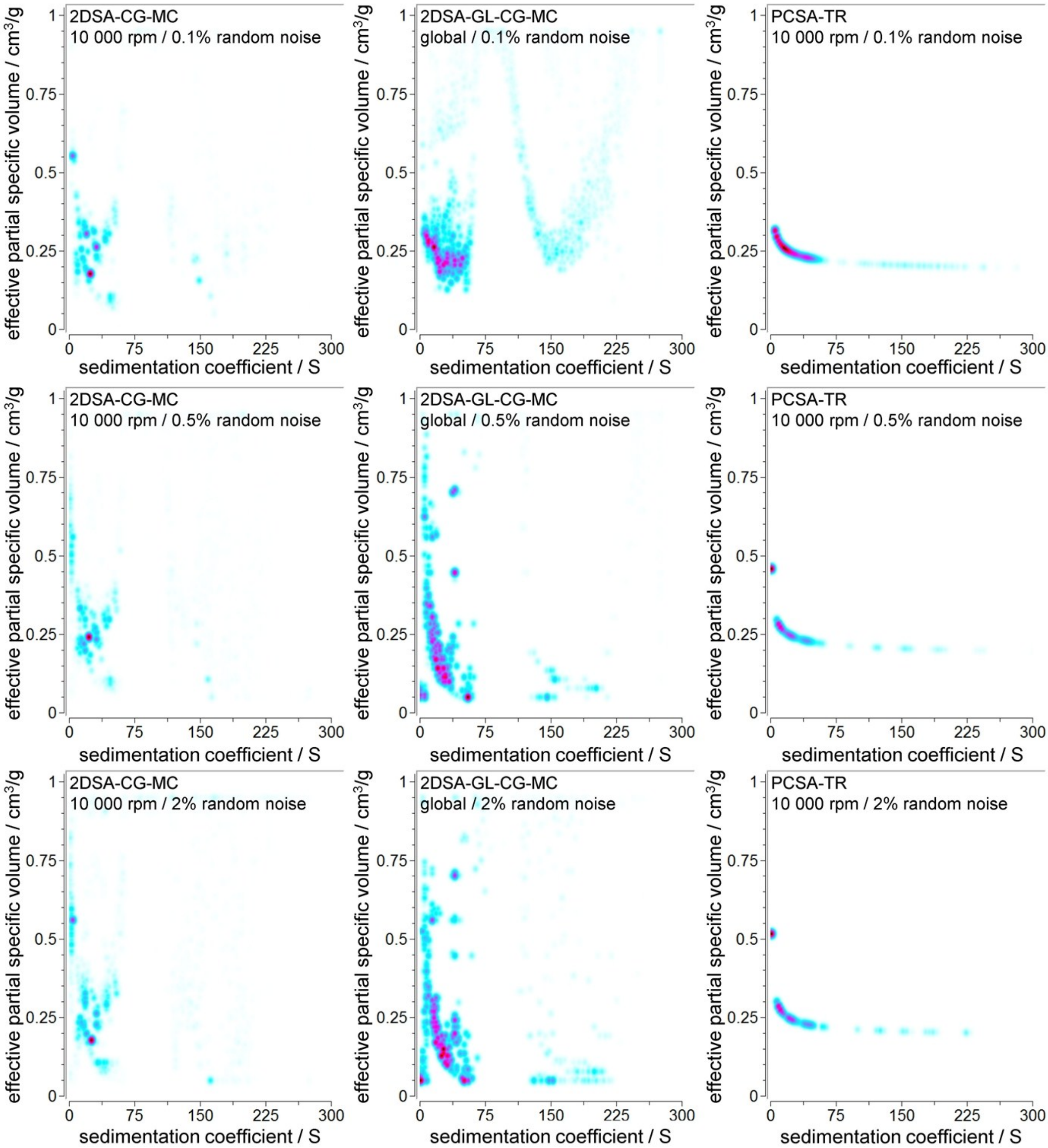

Figure S23. Results of the 2DSA-CG-MC, global speed 2DSA-CG-MC and PCSA-TR shown from left to right for model #3. Results are shown for a rotor speed of 10,000 rpm (except the global speed approach which is a combined analysis at rotor speeds of 10,000 rpm, 20,000 rpm and 40,000 rpm). The random noise is varied top down. The original simulated model to be reproduced (target) is shown in Figure S2.

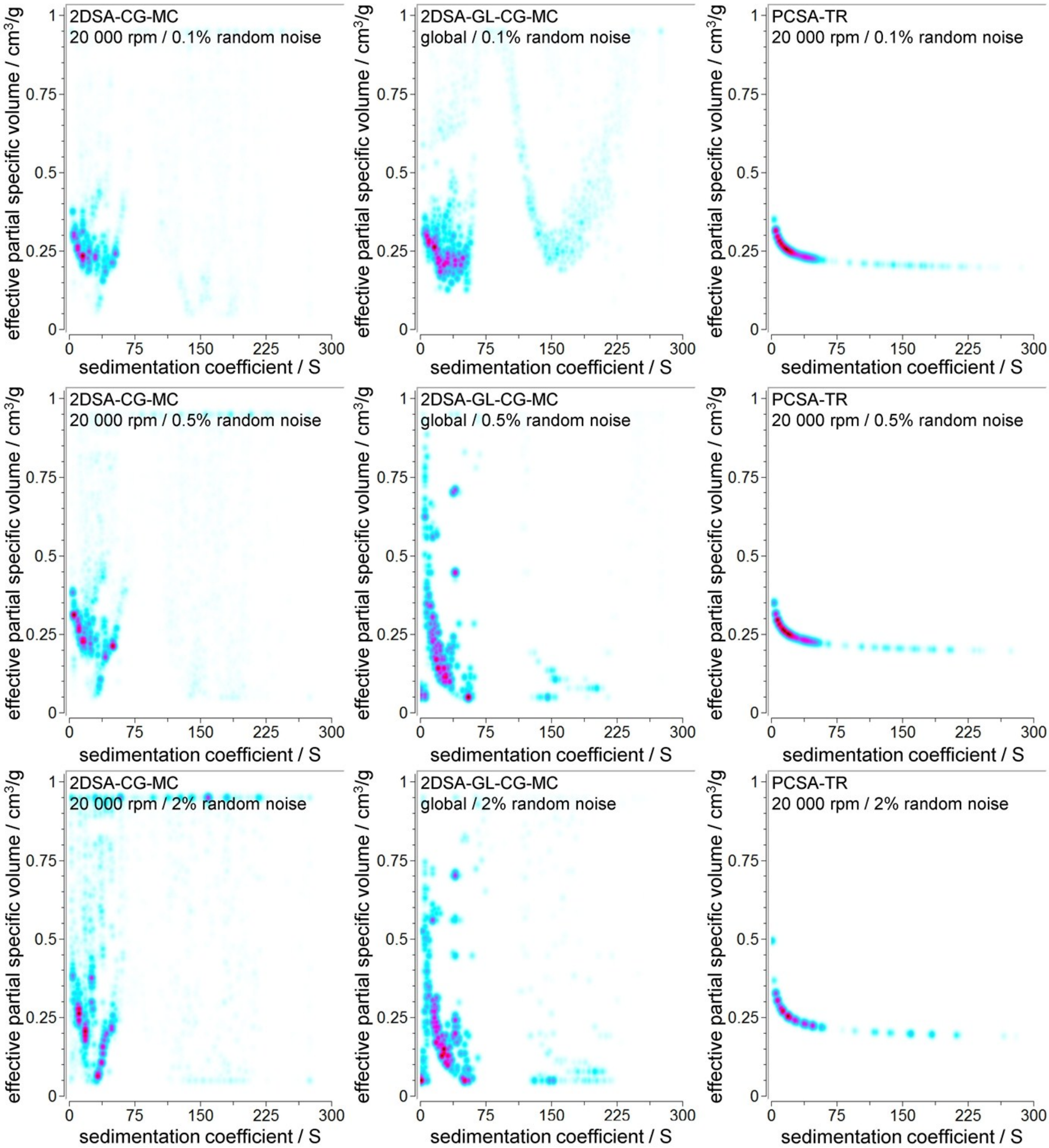

Figure S24. Results of the 2DSA-CG-MC, global speed 2DSA-CG-MC and PCSA-TR shown from left to right for model #3. Results are shown for a rotor speed of 20,000 rpm (except the global speed approach which is a combined analysis at rotor speeds of 10,000 rpm, 20,000 rpm and 40,000 rpm). The random noise is varied top down. The original simulated model to be reproduced (target) is shown in Figure S2.

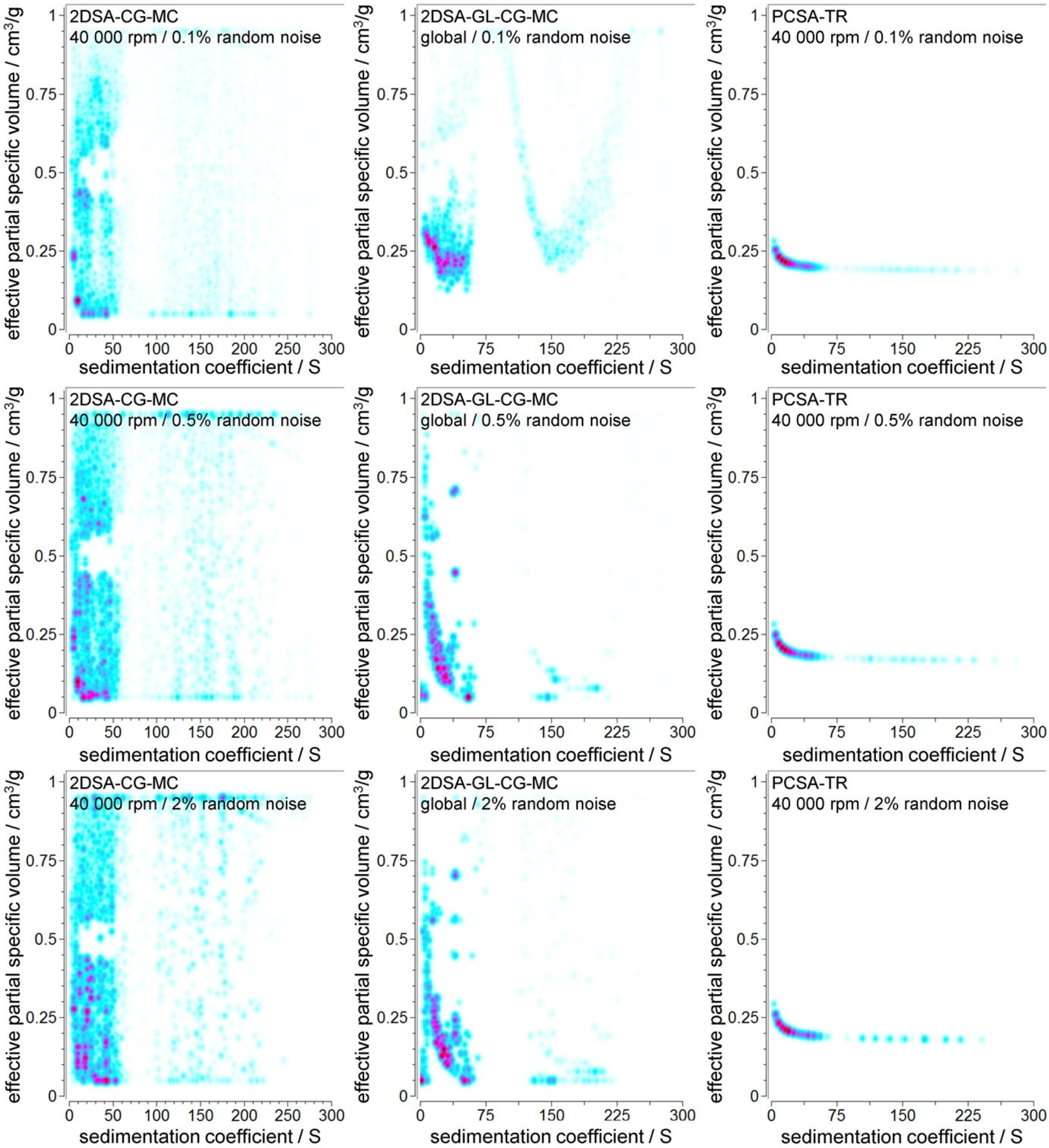

Figure S25. Results of the 2DSA-CG-MC, global speed 2DSA-CG-MC and PCSA-TR shown from left to right for model #3. Results are shown for a rotor speed of 40,000 rpm (except the global speed approach which is a combined analysis at rotor speeds of 10,000 rpm, 20,000 rpm and 40,000 rpm). The random noise is varied top down. The original simulated model to be reproduced (target) is shown in Figure S2.

12 Type of random noise

For the simulated data, random noise proportional to the loading concentration was considered. An alternative would be to simulate random noise proportional to the local concentration. However, such a noise profile can also not be really reflective of the real situation, and in reality is somewhere in between our model and this alternative solution. This is easy to see if one scans a sample at zero concentration. The alternative solution would suggests that the noise at zero would be ideal, i.e., non-existent. This is clearly not the case. In fact, the baseline noise is not much lower than the noise at a slightly higher optical density, say 0.2 OD.

For example, if we measure at 0.2 OD230 nm in our XL-A then the random noise RMSD is about 0.002 OD. If we measure a water channel with zero absorbance, the RMSD is about the same, maybe a little lower at 0.0019 OD. This tells us that a noise contribution based on the percentage of the total loading concentration is not too far off from reality. Once we go to higher concentrations, say 0.9 OD or 1.2 OD the situation is more like what the alternative solution suggests, and the RMSD goes to about 0.004 OD.

Furthermore, the actual noise clearly depends on the background absorbance of the buffer, the wavelength used, the general instrument condition, and condition of monochromator, cell windows, and other optical and electronic components, none of which are predictable nor constant, even within the same machine. For example, the emission intensity varies drastically with wavelength for the Xenon flash lamp used in the UV/Vis detector built into the XL-A, and electronic noise is always finite, and probably the strongest contributor to stochastic noise. In the UV/Vis detection optical system the observed random noise is a combination of lamp flash-to-flash intensity variation, a strong wavelength emission intensity dependence, and the dark current of the detector. Hence, random noise depends on the intensities and thus the wavelength used for data analysis. E.g., for high light intensities, there is almost no variation with the absorbance observable, at least up to a reasonable level (~ 1.0 OD).

These explanations unequivocally illustrate that it is impossible to exactly mimic the influence of random noise in simulated data. A simulation can only provide an estimate of what the impact might be in the analysis. Thus, we decided to provide a worst-case estimate for the studies discussed in this manuscript, which simulates the random noise based on the loading concentration. This allows us to assess the maximum effect of a certain noise level. Of course, the random noise will most likely decrease in reality in the progress of the experiment as the absorbance decreases when the analyte sediments. However, we believe that our procedure is a viable option, which allows us to evaluate the maximum impact of random noise during data analysis.

To show that our worst-case approach is a reasonable procedure, we have performed a simulation based on the assumption that the random noise is proportional to the local concentration instead of the loading concentration. As can be seen in Figure S26, the difference to our noise simulation is either insignificant or the new analysis performs better, which is reasonable due to the overall lower noise values. Moreover, it proves that our original simulation is actually a worst-case scenario, which shows an upper limit of what can be expected when the noise is larger, and does not change our conclusions in any way.

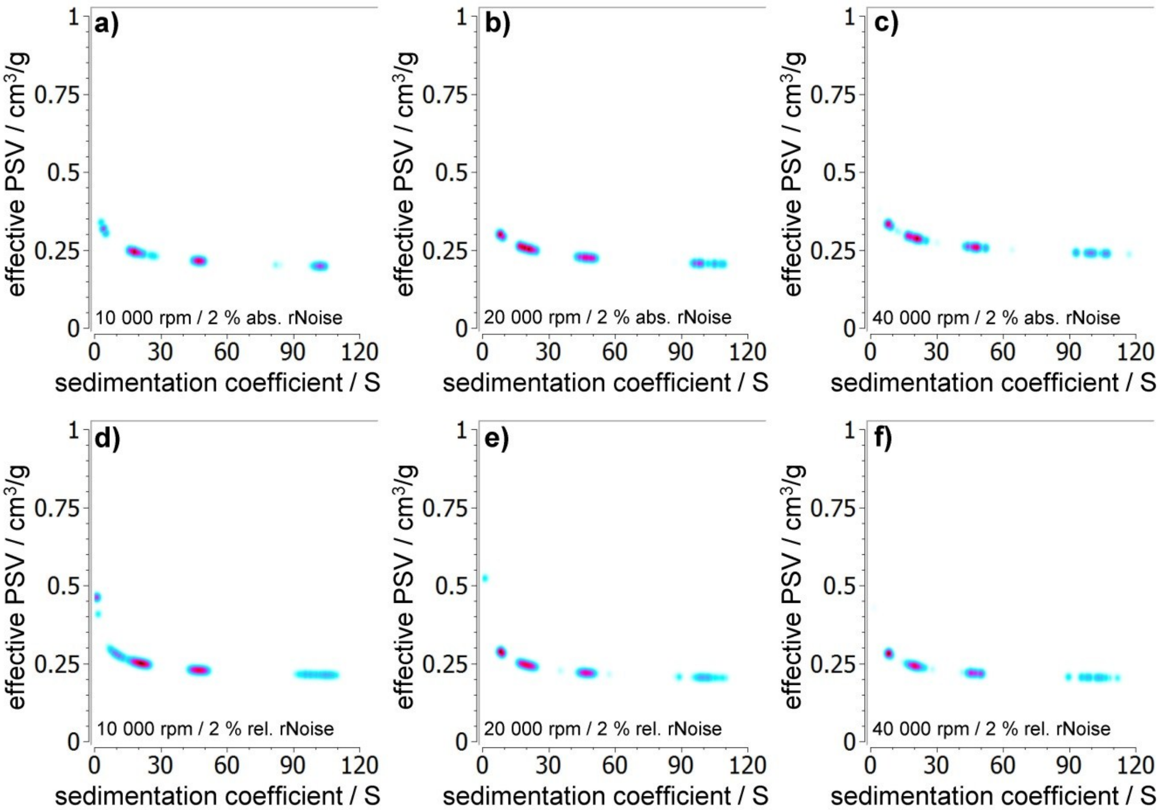

Figure S26. Results of the PCSA-TR shown for model #2 for data simulated at increasing rotor speed from left to right. Data used for analysis shown in a) - c) were simulated with a random noise level of 2 % proportional to the loading concentration of 1.0 OD. Data used for analysis shown in d) - e) were simulated with a random noise level of 2 % proportional to the local concentration. For a rotor speed of 10,000 rpm, the smallest species cannot be well determined due to a lack of sedimentation information available, which holds true for both types of random noise.

13 References

[1] Hubbard, J. B.; Douglas, J. F., Hydrodynamic friction of arbitrarily shaped Brownian particles. *Physical Review E* **1993,** *47* (5), R2983-R2986.